Scanning Probe Lithography Patterning of Monolayer Semiconductors and Its Application for Quantifying Edge Recombination

Peida Zhao[1,2], Ruixuan Wang[1], Der-Hsien Lien[1,2], Yingbo Zhao[1,2], Hyungjin Kim[1,2], Joy Cho[1], Geun Ho Ahn[1,2], and Ali Javey[1,2]*

[1]Electrical Engineering and Computer Sciences, University of California at Berkeley, Berkeley, California 94720, United States

[2]Materials Sciences Division, Lawrence Berkeley National Laboratory, Berkeley, California 94720, United States

Keywords: edge recombination velocity, 2D materials, scanning probe lithography

Abstract

Scanning probe lithography is used to directly pattern monolayer transition metal dichalcogenides (TMDs) without the use of a sacrificial resist. Using an atomic force microscope, a negatively biased tip is brought close to the TMD surface. By inducing a water bridge between the tip and the TMD surface, controllable oxidation is achieved at the sub-100 nm resolution. The oxidized flake is then submerged into water for selective oxide removal which leads to controllable patterning. In addition, by changing the oxidation time, thickness tunable patterning of multilayer TMDs is demonstrated. This resist-less process results in exposed edges, overcoming a barrier in traditional resist-based lithography and dry etch where polymeric byproduct layers are often formed at the edges. By patterning monolayers into geometric patterns of different dimensions and measuring the effective carrier lifetime, the non-radiative recombination velocity due to edge defects is extracted. Using this patterning technique, we show that selenide TMDs exhibit lower edge

recombination velocity as compared to sulfide TMDs. The work highlights the utility of scanning probe lithography towards understanding material dependent edge recombination losses without significantly normalizing edge behaviors due to heavy defect generation, while allowing for eventual exploration of edge passivation schemes which is of profound interest for nanoscale electronics and optoelectronics.

Two-dimensional (2D) monolayer transition metal dichalcogenides (TMDs) possess a variety of unique properties applicable toward different optical and electronic applications.[1-4] Uniquely, the monolayers exhibit self-terminated surfaces without dangling bonds, limiting the number of defects that can exist. However, in contrast to the surface, the edges are filled with dangling bonds which could lead to detrimental effects on device performance.[5-9] For the development of practical 2D nanoelectronics and optoelectronics, the 2D semiconductor is required to be etched to proper nanoscale patterns. This means the formation of edges is inevitable. Moreover, the edge-to-surface ratio will increase with further pattern scaling, causing the problems associated with these edges to become more severe. In that respect, edge effects are important to be quantified and controlled by developing proper etching and passivation schemes. Yet to this day, this remains a largely unexplored research topic. Recently, we introduced a metric to ascertain the edge quality of monolayer TMDs called edge recombination velocity (ERV). Briefly, TMD monolayers are patterned into lateral dimensions where most excitons travel to the edge sites for recombination due to diffusion. ERV is then extracted by measuring the lifetime of monolayer TMDs as a function of patterned dimensions using time-resolved photoluminescence (TRPL).[10] The ideal edge patterning technique should not significantly impact the edge properties of different TMDs during the fabrication process. Specifically, the traditionally explored resist-based lithography and plasma dry etching processes often leave a polymeric byproduct layer at the patterned edges, which limits study of the intrinsic edge properties. The mitigation of fabrication-induced defects will allow us to understand intrinsic material dependent edge property variations instead. One promising technique to overcome this problem is scanning probe lithography (SPL)[11, 12], where surface patterning is conducted by applying a voltage between a probe tip and the substrate without the use of a sacrificial resist.

In this work, we utilize SPL to pattern monolayers of MoS_2, $MoSe_2$, WS_2, and WSe_2 on SiO_2/Si substrates while investigating the various parameters that can affect the patterning process. These parameters include tip bias, dwell time, humidity, and setpoint amplitude. By fine tuning these parameters, we demonstrate a patterning resolution of <100 nm and a thickness dependent oxidation of thicker TMDs through variation of tip dwell time. To ascertain the edge quality of monolayer TMDs, edge recombination velocity (ERV) – a metric that we have previously introduced – is utilized.[10] In this study, we extract ERVs of four TMDs (MoS_2, $MoSe_2$, WS_2 and WSe_2) patterned *via* SPL. Compared to the extracted ERV of WS_2 fabricated with e-beam lithography in a previous study, we observe lower ERV and higher edge lifetime (τ_{edge}). In addition, the selenides are found to exhibit lower ERVs compared to sulfides. We also show that it is possible to passivate the edges by chemical treatment as the edges formed by SPL are exposed without any residual coating.

Experimental Section

Figure 1a and 1b illustrate the SPL for patterning monolayer TMDs (preparation of TMD materials is shown in the Supporting Information) *via* atomic force microscope (AFM). During lithography, a diamond-like-carbon (DLC) coated silicon tip (Bruker, DDESP-V2) is brought close to the surface (with an amplitude setpoint of ~0.6 nm) while a voltage is applied across from the tip (V_{tip} = -12 V) to the Si substrate (V_{sub} = 10 V). Precise tip movements during SPL are captured *via* AFM's high speed data capture card and are included in Figure S1. The AFM chamber is also maintained at <25% humidity. After oxidation, the entire flake is submerged in DI water, where the oxidized region is selectively removed while leaving the rest of the flake intact. Figure 1c shows a MoS_2 monolayer patterned into grids of three different sizes – 1 µm, 500 nm and 250 nm

respectively – using SPL. Notably, the monolayers are patterned on a SiO_2/Si substrate rather than on a conductive substrate, where the voltage is capacitively coupled through the insulating substrate. The use of a SiO_2/Si substrate provides a more practical platform for optoelectronic characterization and device applications.

SPL lithography consists of two parts – TMD oxidation and selective oxide removal via water. To enable oxidation, a water bridge first forms between the AFM tip and the TMD surface *via* a voltage application at the AFM tip. The oxidation reaction proceeds as: [11, 13-15]

$$MX_2 + x\,H_2O \leftrightarrow MO_x + y\,H_2 + XO_y \qquad (1)$$

where M stands for the transition metal of interest, and X the chalcogen of interest. x and y take on different values depending on the specific TMD in question. After oxidation, the sub-stochiometric transition metal oxides can be removed *via* water as reported elsewhere.[11, 16]

To elucidate the oxidation mechanism, we focus on appropriate conditions when water bridge formation is favorable. The resultant oxidation area (or SPL resolution) is directly related to the water bridge coverage area over the TMD surface. While the details of the water bridge formation is described elsewhere,[17] we qualitatively relate the key experimental parameters with known model to establish consistency.

Generally, water bridge formation is favorable when the following energy relation is satisfied:

$$\Delta U = U\,(\text{water bridge}) - U_o\,(\text{vapor}) = \Delta U_s + \Delta U_c + \Delta U_{vdW} + \Delta U_e < 0 \qquad (2)$$

$$\text{where } \Delta U_e\,(V_{tip}),\ \Delta U_c\,(RH),\ \Delta U_{vdW}\,(V_{setpoint}) \qquad (3)$$

The potential energy difference, ΔU, shows a competitive process between water condensation and water vapor formation. To determine whether a bridge forms, the surface energy (U_s),

condensation energy (U_c), van der Waals energy (U_{vdW}), and electrostatic energy (U_e) of the system is summed together. When $\Delta U < 0$, the water bridge forms. As ΔU becomes more negative (or more favorable for water bridge formation), the water bridge also increases in width, resulting in a larger TMD surface coverage, larger oxidized area and lower SPL resolution. We expect increasing tip bias V_{tip} (increasing ΔU_e), decreasing tip to surface distance (increasing ΔU_{vdW}) and increasing humidity (decreasing ΔU_c) to all contribute to a more stable, and wider water bridge formation.

The impacts of the mentioned parameters are shown in **Figure 2**. Figure 2a shows the impact of tip bias V_{tip} on the oxidation process. When V_{tip} changes from -12V to -2V, the oxidized area becomes smaller, implying a smaller water bridge with reduced V_{tip}. This is expected as V_{tip} affects the water bridge formation *via*[17]:

$$U_e = \frac{\varepsilon_o}{2} \int_V \varepsilon |\boldsymbol{E}|^2 dv \qquad (4)$$

Here $\varepsilon_o$is the vacuum permittivity, $\boldsymbol{E}$ is the space-varying (or tip-induced) electric field, ε is the relative permittivity of the relevant liquid (water), and V is the volume of the condensed liquid. Figure S4. illustrates approximate shape of the meniscus before water bridge formation and the relevant integral volume. It can been seen that at a smaller V_{bias}, the electric field $\boldsymbol{E}$ between the tip and TMD surface is smaller, leading to a smaller U_e. From equation (2) we see that a smaller ΔU_e (when a tip bias is applied vs. when a tip bias is not applied) minimizes $|\Delta U|$, correlated to a smaller water bridge formation and consistent with Figure 2a.

Next, the impact of amplitude setpoint, $V_{setpoint}$, on oxidation is investigated. $V_{setpoint}$ is the feedback parameter that AFM attempts to maintain during SPL and is related to the tip-to-TMD surface vdW force. The voltage value refers to the tip amplitude oscillation at a fixed drive

amplitude of the piezo element, with a smaller oscillation achieved by tip lowering to maintain surface tracking. Changing the voltage setpoint directly decreases or increases the distance of the tip to TMD surface and changes the vdW force experienced between the two interfaces. The vdW force between water molecules can be described *via* the following relation[17]:

$$U_{vdw} = \frac{H}{12\pi}\int_S \frac{1}{\xi^2} ds \qquad (5)$$

where H is the Hamaker constant, S is the surface area of the TMD/water interface, and ξ is a distance between the top and bottom surfaces of the water bridge. We see in equation (5) that the tip-surface distance enters into the vdW energy calculation *via* ξ, where a larger separation translates to a smaller U_{vdW} and vice versa. Therefore, we expect that a lower setpoint during lithography will lead to a larger oxidized area (due to a more stable and larger water bridge) while a higher setpoint leads to a smaller oxidized area. Figure 2 b confirms this expectation as we change the tip-to-surface distance from 0.63 nm to 4.4 nm (directly corresponding to the appropriate $V_{setpoint}$).

Lastly, relative humidity, RH, is defined as the ratio between water vapor concentration in the air normalized to the saturation concentration of water vapor. RH influences the oxidation process by controlling the condensation energy (U_c) where the following relation applies[17]:

$$U_c = \frac{R_g T}{v_m} \ln\left(\frac{1}{\mathrm{RH}}\right)\int_V dv \qquad (6)$$

where R_g is the gas constant, T is the temperature, and v_m is the molar volume of liquid. The condensation energy is also evaluated over the volume of the condensed liquid V present similar to equation 4 and illustrated in Figure S4. Note that the above relation only holds for water vapor before supersaturation; for condensation of other liquids, RH becomes a ratio of vapor pressure at the condition of interest divided by vapor pressure at saturation.

From equation (6), we expect very limited oxidation (therefore very small water bridge formation) at lower humidity. Lower RH translates into a higher U_c, implying difficulty in liquid condensation and easier vapor formation. Qualitatively, lower RH means a drier environment, which drives water vapor formation over condensation. As U_c increases, ΔU from equation (2) becomes more positive, translating to a smaller water bridge coverage. Conversely, water bridge width should increase at higher RH, leading to an increased oxidation area. Interestingly, continuous incremental increase in RH results in a slower incremental increase of the oxidation area due to the natural log function. Figure 2c substantiates this hypothesis and demonstrates a significant difference in the oxidation area as RH changes from <5% to 25%, and a much smaller difference (if any) in oxidation size between 25% to 45% humidity.

After examining the water bridge formation mechanism, we discuss the oxidation process. V_{tip} can be either positive or negative (with respect to the TMD surface) for a successful water bridge formation.[17] However, negative V_{tip} is needed to induce the oxidation reaction. While some TMDs (MoS_2, $MoSe_2$, WS_2, and WSe_2 being the relevant TMD members) spontaneously oxidize under ambient conditions (at a very slow rate),[13, 14] we postulate that the negative tip bias supplies a larger amount of OH^- from the water bridge to the TMD surface, speeding up the general reaction detailed in equation (1). Furthermore, the Fermi level of the TMD is moved by the applied voltage which further reduces the oxidation energy.

Finally, by optimizing the various parameters discussed above, we demonstrate the smallest dimension of dots and lines achievable *via* SPL in Figure 2d. Both the line width and the dot diameters are < 100 nm. The condition is set at V_{tip} = -2 V (with a substrate bias of 10 V), $V_{setpoint}$ = 30 mV, and RH ~ 35%. Any further efforts at reducing the SPL resolution leads to inconsistencies in the line patterning. Smaller dimension has been reported *via* SPL on TMDs

elsewhere, and we attribute other factors (such as tip radius, tip type, and differences in the surface energies ΔU_s) to also play a role in reaching the highest resolution possible.[11]

In tuning various SPL parameters for oxidation, we find an interesting effect of oxidation dwell time t_{dwell} in relation to multilayer TMDs. While the impact of t_{dwell} is not explicitly included in equation (2), longer t_{dwell} should give more time for oxidation to complete at a specific water bridge size. While the impact of t_{dwell} is harder to observe for monolayer TMDs (due to the relatively short time a monolayer can be completely oxidized), thicker TMDs need more time to fully oxidize. Therefore, a thickness dependent oxidation effect can be observed as we scan t_{dwell}, specifically for thicker TMDs. **Figure 3** shows a time dependence of the oxidation process for both monolayers and multilayer TMDs.

For monolayers, t_{dwell} starts having negligible effects on the oxidation pattern after a slight increase in oxidized area going from 4-6 seconds. This is most likely because monolayer oxidation under the water bridge completes quickly (< 4 seconds), and vertical oxidation dependence is hard to observe at the monolayer thickness. Note that because t_{dwell} is not included in Equation 2, the size of the water bridge formed should be the same for all different t_{dwell} cases, leading to similarly sized monolayer oxidation. Figure 3b shows the same dwell time variation applied to thicker TMD layers. Here, a clear depth dependence is seen when t_{dwell} increases. Similar to SPL oxidation of silicon[18, 19], deeper layers of TMDs are oxidized at longer t_{dwell}, resulting in thicker oxides accompanied by a deeper trench after water submersion shown in Figure 3c. This oxidation depth dependence on t_{dwell} also highlights the potential of SPL used towards controllable layer-by-layer oxidation of thicker TMDs for various applications.

Compared to the more commonly used lithography techniques (such as photo- or e-beam lithography combined with wet or dry etching), SPL (combined with water removal) can avoid

many nonidealities such as resist residues, electron backscattering effects, and etching-related contaminations.[20, 21] Therefore, we use SPL to pattern monolayer MoS_2, $MoSe_2$, WS_2, and WSe_2 TMDs in the same fashion shown in Figure 1c, and measure their respective ERVs to assess their intrinsic edge qualities.

Briefly, all four TMDs are patterned down into square arrays with three different length l (1 µm, 500 nm and 250 nm). As l decreases, the increased circumference to surface area ratio means a higher contribution of the edge recombination effects, resulting in lower photoluminescence (PL) intensity after fill factor corrections (Figure S2). Utilizing TRPL for lifetime measurements, we identify the lower carrier concentration regime (at ~10^{-1} W/cm^2 power density for all four TMDs) to extract the relevant effective lifetimes.[22, 23] The effective lifetime ($\tau_{effective}$) is broken down into a surface lifetime ($\tau_{surface}$) and an edge lifetime (τ_{edge}):

$$\frac{1}{\tau_{effective}} = \frac{1}{\tau_{surface}} + \frac{1}{\tau_{edge}} \quad (7)$$

The surface lifetimes are measured on unetched monolayers as 1.5, 10.9, 1.18, and 0.9 ns for MoS_2, $MoSe_2$, WS_2, and WSe_2 respectively. τ_{edge} is then extracted and correlated to ERV via equation (8). Due to the square cross sections of the flake, the geometric correction factor relating ERV to τ_{edge} derivation changes slightly as compared to our previously reported work using disks[10] with details included in supporting information:

$$\tau_{edge} = \frac{l}{2 \times \mathrm{ERV}} \quad (8)$$

Extraction of MoS_2 ERV proves particularly challenging. **Figure 4**a shows the TRPL of MoS_2 for various sizes, including an unetched monolayer control. In addition to the lifetime being close to the instrument response function (which is remedied by employing iterative re-

convolution), the unetched control $\tau_{effective}$ is very close to that of the etched samples of all three sizes. This introduces a very large error in τ_{edge} extraction using equation (3). A more accurate extraction of τ_{edge} therefore requires that $\tau_{surface} \gg \tau_{effective}$, or where length dependence is clearly observed from the TRPL series.

Since the entire SPL process only involves DI water removal after oxidation and does not use any polymeric based resist/organic chemicals, the resulting edges are free of polymeric byproducts often observed in dry etching processes. By employing a previously known passivation scheme, $\tau_{surface}$ of a SPL-patterned MoS_2 monolayer can be improved with bis(trifluoromethane) sulfonimide (TFSI).[22] Figure 4b shows the TRPL of the sample after TFSI treatment with the corresponding ERV shown in Figure 4c. In contrast, no lifetime change with chemical treatment is observed in samples patterned with standard resist-based lithography and plasma dry etching.[10]

Figure 5 a-c shows the TRPL of WSe_2, WS_2, and $MoSe_2$ respectively, and the extracted ERVs of the four studied TMDs are shown in in Figure 5d. Individual TMD steady state PL and ERV extractions are detailed in Figure S2-3. The extracted ERVs are 2×10^4 cm/s, 2.6×10^3 cm/s, 1.8×10^4 cm/s and 1.1×10^4 cm/s for MoS_2, $MoSe_2$, WS_2, and WSe_2 respectively. From our previous work, WS_2 edges made with resist-based e-beam lithography has a measured ERV of 4×10^4 cm/s. Compared to the SPL WS_2 ERV of 1.8×10^4 cm/s measured here, we observe a > 2x improvement with τ_{edge} improving from 0.2-0.3 ns to 1.1 ns (Figure S3d) at 500 nm length regime extracted *via* TRPL.[10] As expected, the ERV varies between different etching processes due to the different defect densities introduced by each process and potential passivation effect from resist residue.

Other works have shown TMD selenides to possess longer surface lifetime. Interestingly, $MoSe_2$ ERV is approximately an order smaller than the other three TMDs, and quite clearly mimics the material's surface properties. This ERV variation corresponds clearly to the much longer $\tau_{surface}$ of $MoSe_2$ (~116 ns) compared to the $\tau_{surface}$ of the other three TMDs (~3 ns, ~10 ns, and ~20 ns for WS_2, MoS_2 with TFSI, and WSe_2 respectively).[23] This large ERV variation highlights the differences in edge properties as a function of the material rather than the etching process. Therefore, SPL demonstrates itself as an ideal lithography method for future ERV study due to the observable material dependent edge variations after patterning.

In conclusion, an in-depth investigation of the various parameters affecting SPL patterning of TMDs is discussed. Voltage bias, amplitude setpoint, and humidity have all shown tunability on TMD monolayer oxidation and are consistent with known theory, reaching sub-100nm resolution. The oxidized area can be selectively removed via water to complete the lithography process. In addition, SPL dwell time can used to control the thickness of oxidized multilayer TMDs, demonstrating the possibility of layer-by-layer oxidation control. Finally, SPL has been used to extracted the ERV of four different TMD materials MoS_2, $MoSe_2$, WS_2, and WSe_2. Due to the lack of exposure to resist or plasma species, the process yields material dependent edges properties, reinforcing SPL as an attractive patterning technique for future edge passivation studies and comparative edge structure characterizations.

Supporting Information

See supporting information for the highspeed data capture of AFM during SPL, preparation of materials, steady state PL spectra of $MoSe_2$, MoS_2, WSe_2, and WS_2 as a function of size, extracted τ_{edge} of all four aforementioned materials, and derivation of ERV relation for square cross sections. Supporting Information is available from the Wiley Online Library or from the author.

Acknowledgements

We thank Shiekh Z. Uddin for assistance with theory and modeling. Scanning probe lithography and processing of monolayers were supported by NSF E3S Center. PL and TRPL measurements were supported by the Electronic Materials Program, funded by Director, Office of Science, Office of Basic Energy Sciences, Materials Sciences and Engineering Division of the U.S. Department of Energy under contract no. DE-AC02-05Ch11231.

References

[1] S. B. Desai, S. R. Madhvapathy, A. B. Sachid, J. P. Llinas, Q. Wang, G. H. Ahn, G. Pitner, M. J. Kim, J. Bokor, C. Hu, H. S. P. Wong, A. Javey, *Science* **2016,** *354*, 99.

[2] D.-H. Lien, M. Amani, S. B. Desai, G. H. Ahn, K. Han, J.-H. He, J. W. Ager, M. Wu, C. A. Javey, *Nat. Commun.* **2018,** *9*, 1229.

[3] M. Tosun, S. Chuang, H. Fang, A. B. Sachid, M. Hettick, Y. Lin, Y. Zeng, A. Javey, *ACS Nano* **2014,** *8*, 4948-4953.

[4] F. Withers, O. Del Pozo-Zamudio, A. Mishchenko, A. P. Rooney, A. Gholinia, K. Watanabe, T. Taniguchi, S. J. Haigh, A. K. Geim, A. I. Tartakovskii, K. S Novoselov, *Nat. Mater.* **2015,** *14*, 301.

[5] W. Bao, N. J. Borys, C. Ko, J. Suh, W. Fan, A. Thron, Y. Zhang, A. Buyanin, J. Zhang, S. Cabrini, P. D. Ashby, A. Weber-Bargioni, S. Tongay, S. Aloni, D. F. Ogletree, J. Wu, M. B. Salmeron, P. J. Schuck, *Nat. Commun.* **2015,** *6*, 7993.

[6] Q. Chen, H. Li,; W. Xu, S. Wang, H. Sawada, C. S. Allen, A. I. Kirkland, J. C. Grossman,; J. H. Warner, *Nano Letters* **2017,** *17*, 5502-5507.

[7] M. H. D. Guimarães, H. Gao, Y. Han, K. Kang, S. Xie, C.-J. Kim, D. A. Muller, D. C. Ralph, J. Park, *ACS Nano* **2016,** *10*, 6392-6399.

[8] M. S. Kim, S. J. Yun, Y. Lee, C. Seo, G. H. Han, K. K. Kim, Y. H. Lee, J. Kim, *ACS Nano* **2016,** *10*, 2399-2405.

[9] J. S. Ross, P. Klement, A. M. Jones, N. J Ghimire,. J. Yan, D. G. Mandrus, T. Taniguchi, K. Watanabe, K. Kitamura, W. Yao, D. H. Cobden, X. Xu, *Nat. Nanotech.* **2014,** *9*, 268.

[10] P. Zhao, M. Amani, D.-H. Lien, G. H. Ahn, D. Kiriya, J. P. Mastandrea, J. W. Ager, E. Yablonovitch, D. C. Chrzan, A. Javey, *Nano Lett.* **2017,** *17*, 5356-5360.

[11] A. I. Dago, Y. K. Ryu, R. Garcia, *Appl. Phys. Lett.* **2016,** *109*, 163103.

[12] F. M. Espinosa, Y. K. Ryu, K. Marinov, D. Dumcenco, A. Kis, R. Garcia, *Appl. Phys. Lett.* **2015,** *106*, 103503.

[13] S. Kc, R. C. Longo, R. M. Wallace, K. Cho, *J. Appl. Phys.* **2015,** *117*, 135301.

[14] X. Zhang, F. Jia, B. Yang, S. Song, *J. Phys. Chem. C* **2017,** 121, (18), 9938-9943.

[15] H. Liu, N.Han, J. Zhao, *RSC Adv.* **2015,** *5*, 17572-17581.

[16] Bothra, S. Sur, H. Liang, V. *Microelectron. Reliab.* **1999,** *39*, 59-68.

[17] T. Ondarcuhu, J.-P. A., *Nanoscale Liquid Interfaces: Wetting, Patterning and Force Microscopy at the Molecular Scale*. 1 ed. Pan Stanford: New York, 2013.

[18] P.Avouris, R. Martel, T. Hertel, R. Sandstrom, *Appl.Phys. A* **1998,** *66*, S659-S667.

[19] Y.-R. Ma, C. Yu, Y. D. Yao, Y. Liou, S. F. Lee, *Tip-induced local anodic oxidation on the native SiO2 layer of Si (111) using an atomic force microscope*. 2001 Vol. 64.

[20] T. Kamikubo, T. Abe, S. Oogi, H. Anze, M. Shimizu, M. Itoh, T. Nakasugi, T. Takigawa, T.Iijima, Y. Hattori, T. Tojo. *J. J. Appl. Phys.* **1997,** *36*, 7546.

[21] J. D. Plummer, M. D. D., Peter B. Griffin, *Silicon VLSI Technology: Fundamental, Practice, and Modeling*. Pearson Education: India, 2009.

[22] M. Amani, D.-H. Lien, D. Kiriya, J. Xiao, A. Azcatl, J. Noh, S. R. Madhvapathy, R. Addou, S. Kc, M. Dubey K., Cho, R. M. Wallace, S.-C. Lee, J.-H. He, J. W. Ager, X. Zhang, E. Yablonovitch, A. Javey, *Science* **2015,** *350*, 1065.

[23] M. Amani, P. Taheri, R. Addou, G. H. Ahn, D. Kiriya, D.-H. Lien, J. W. Ager, R. M. Wallace, A. Javey, *Nano Lett.* **2016,** *16*, 2786-2791.

Figures

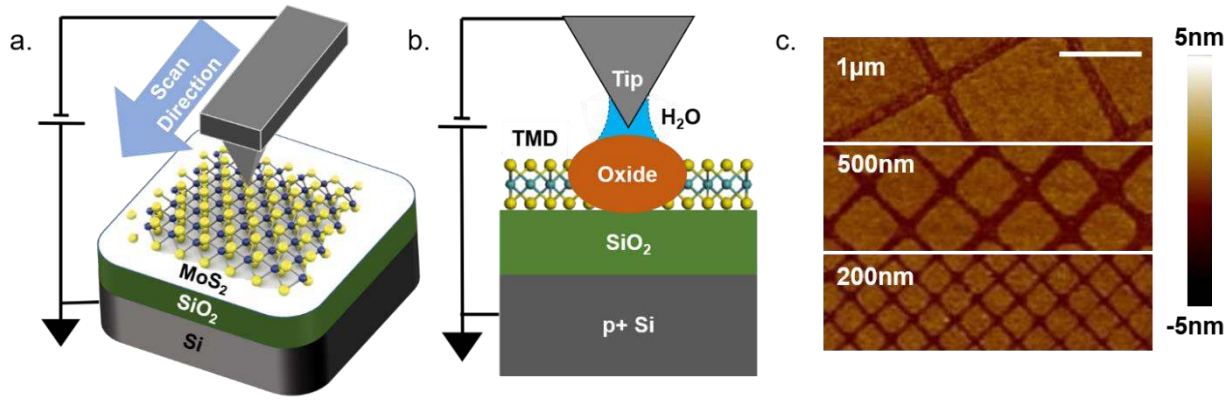

Figure 1. a) A representative schematic of the SPL patterning of a MoS_2 monolayer. b) The sideview illustration, depicts the formation of a water bridge between the tip and the monolayer as a bias is applied, leading to the local oxidation of the monolayer. c) AFM images of a MoS_2 monolayer patterned into grids of different dimension after water removal of the MoO_x patterned area. Scale bar represents 500nm.

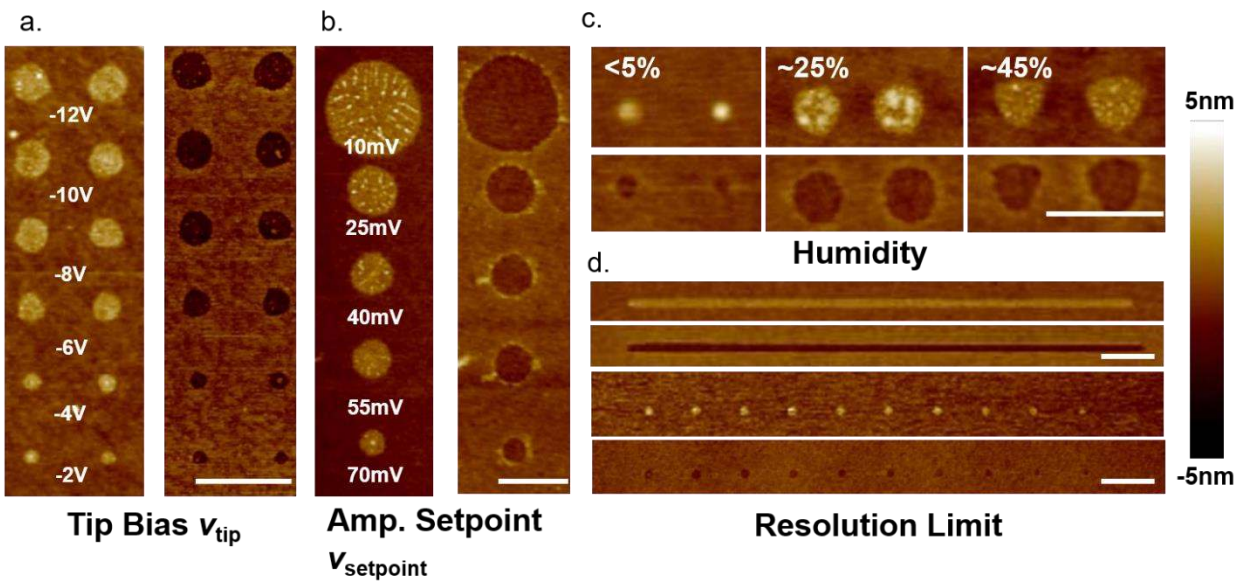

Figure 2. Effects of changing SPL process parameters on the patterning resolution of TMD monolayers. a) Tip voltage bias variation; higher tip voltage corresponds to a larger oxidation area (left panel) and subsequently a larger patterned area after oxide removal by water (right panel). b) Amplitude setpoint variation; the closer the tip approaches the surface, the larger the oxidized spot (left panel) and the correspondingly larger patterned area after oxide removal (right panel). c) Humidity variation; adequate oxidation dot size requires a high enough humidity, where above the threshold humidity level, beyond which no significant variation in oxidation size exists. d) Finest resolution limit achievable *via* SPL, showing both dots and lines at <100 nm resolution respectively by tuning all parameters. For all the dots/circles, the tip is held at a constant position on the monolayer. For the lines, the tip is scanned along a single axis. Scale bar is 500 nm.

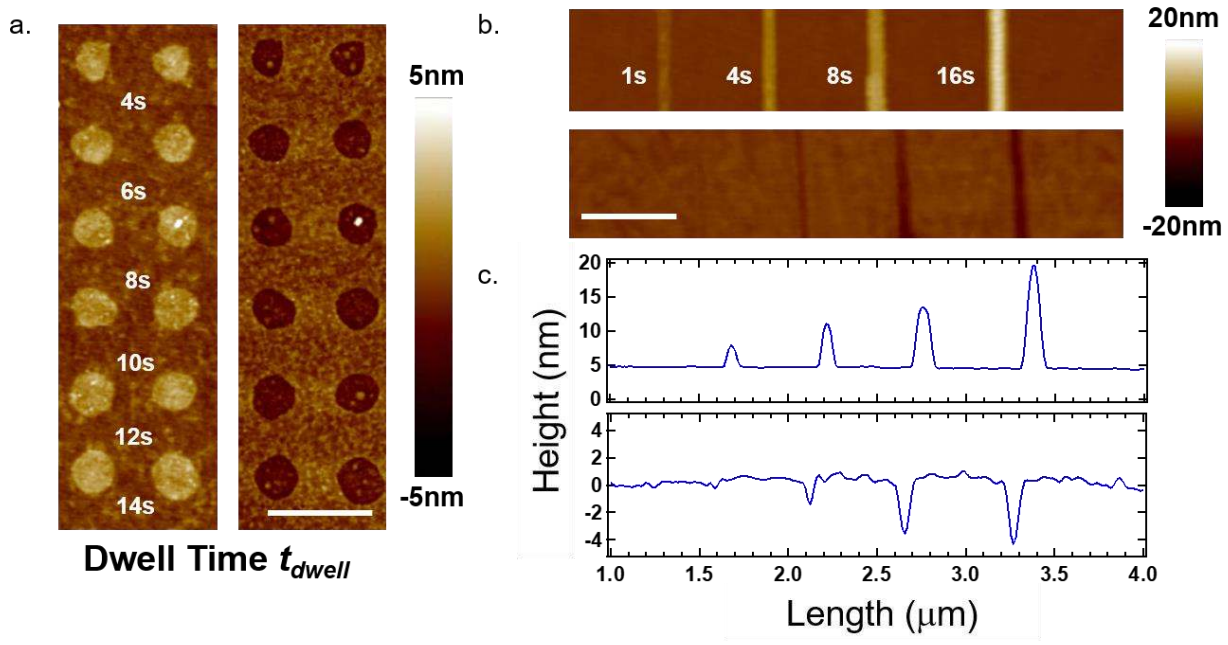

Figure 3. Dwell time effects on SPL patterning of monolayer and multilayer MoS_2. a) Dwell time effect on monolayer patterning, before (left panel) and after (right panel) water removal of the oxide. Dwell time has minimal effect on the oxidation area for the explored dwell time range. b) Dwell time effect on multilayer (< 50 nm in thickness) patterning. Increasing dwell time increases the oxidation depth. Four different t_{dwell} are used on a TMD multilayer, where each successive increase shows a thicker oxidation (top panel) and deeper trenches (bottom panel) after water removal of the oxide. c) AFM height scan of the TMD surface presented in b) after oxidation (top panel) and water removal of the oxide (bottom panel). Scale bar is 500 nm.

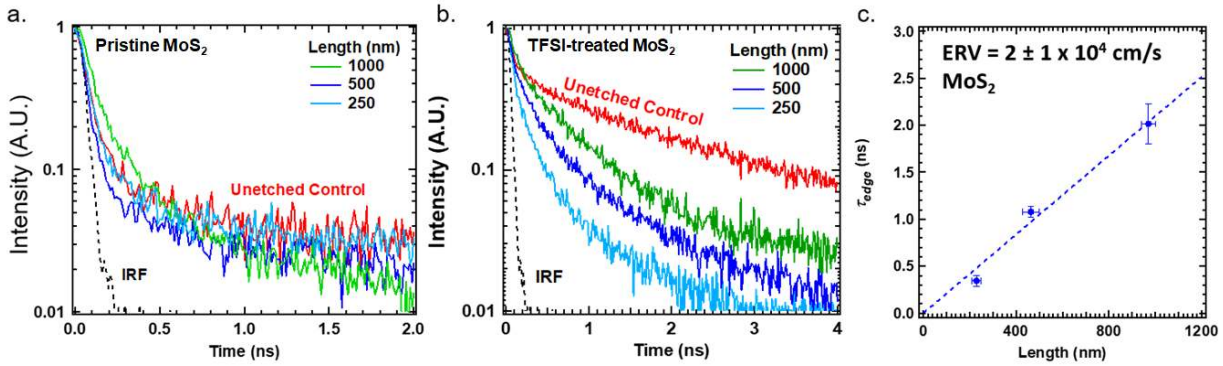

Figure 4. Edge recombination velocity extraction of MoS_2. a) TRPL of MoS_2 squares of varying lengths of 250 nm, 500 nm and 1 µm, including an unetched control sample. b) TRPL of the same MoS_2 samples after TFSI treatment. c) Length dependence of t_{edge} for TFSI-treated MoS_2, yielding an ERV ~ 2 x 10^4 cm/s.

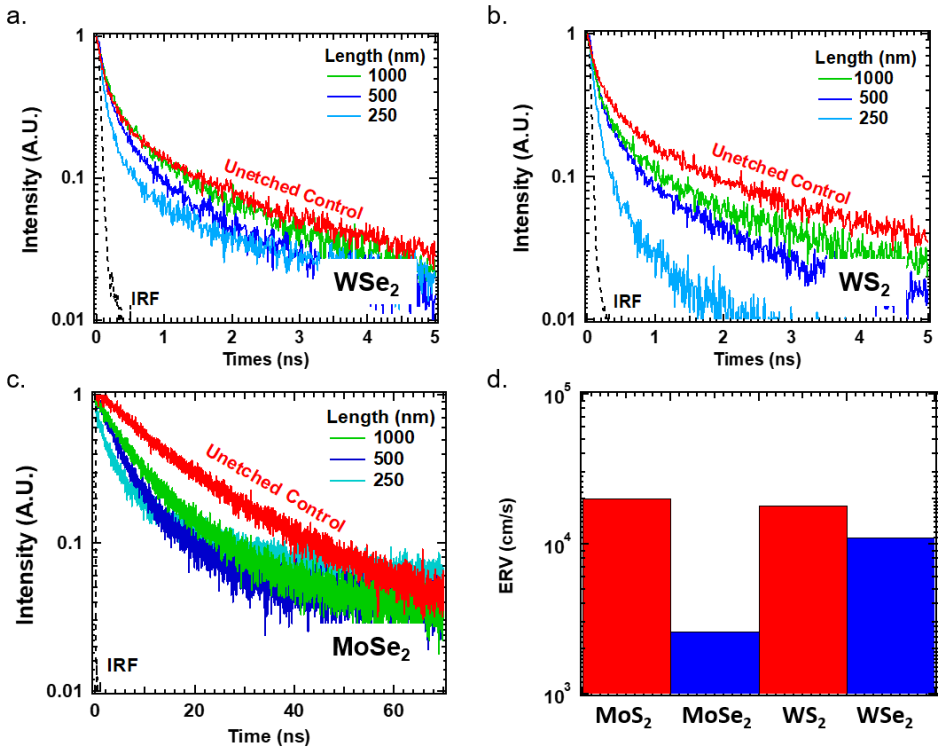

Figure 5. Time resolved photoluminescence measurements of SPL patterned squares of a) WSe_2, b) WS_2 and c) $MoSe_2$. d) Extracted edge recombination velocity for all four TMDs. Selenium based compounds are observed to have relatively lower ERVs compared to the sulfides.

Supporting Information

Scanning Probe Lithography Patterning of Monolayer Semiconductors and Its Application for Quantifying Edge Recombination

Peida Zhao[1,2], Ruixuan Wang[1], Der-Hsien Lien[1,2], Yingbo Zhao[1,2], Hyungjin Kim[1,2], Joy Cho[1], Geun Ho Ahn[1,2], and Ali Javey[1,2]*

[1] Electrical Engineering and Computer Sciences, University of California at Berkeley, Berkeley, California 94720, United States

[2] Materials Sciences Division, Lawrence Berkeley National Laboratory, Berkeley, California 94720, United States

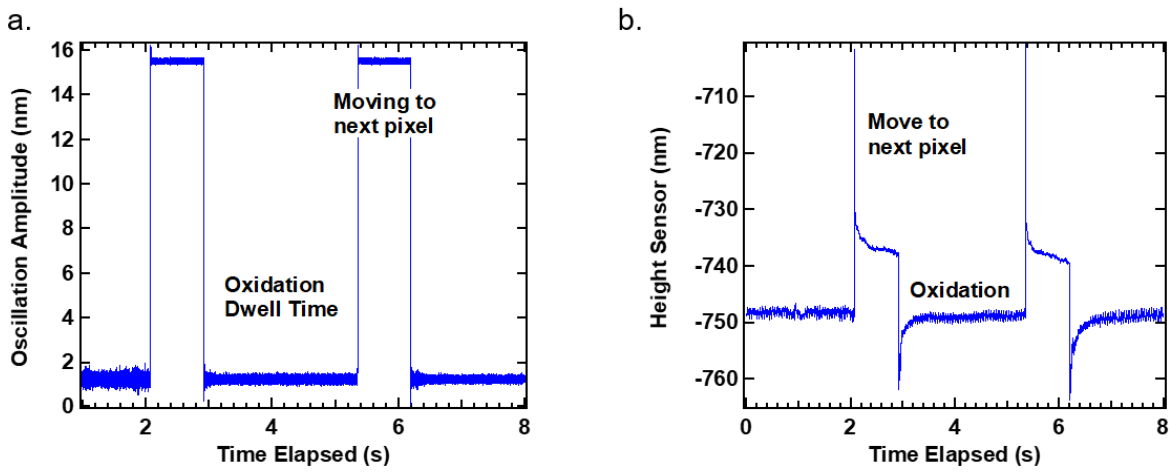

Figure S1. Highspeed Data Capture of AFM sensors during the SPL process. a) Oscillation amplitude for the AFM tip - very little oscillation happens during the writing process due to the tip proximity to the sample surface (each dot took ~1 second to oxidize in this example), while the tip returns to a standard tapping mode oscillation when moving from one pixel to another. b) Tip height during a write sequence. The tip generally remains ~15 nm away from the surface when moving from pixel to pixel, while it stays very close to the surface during the actual oxidation process.

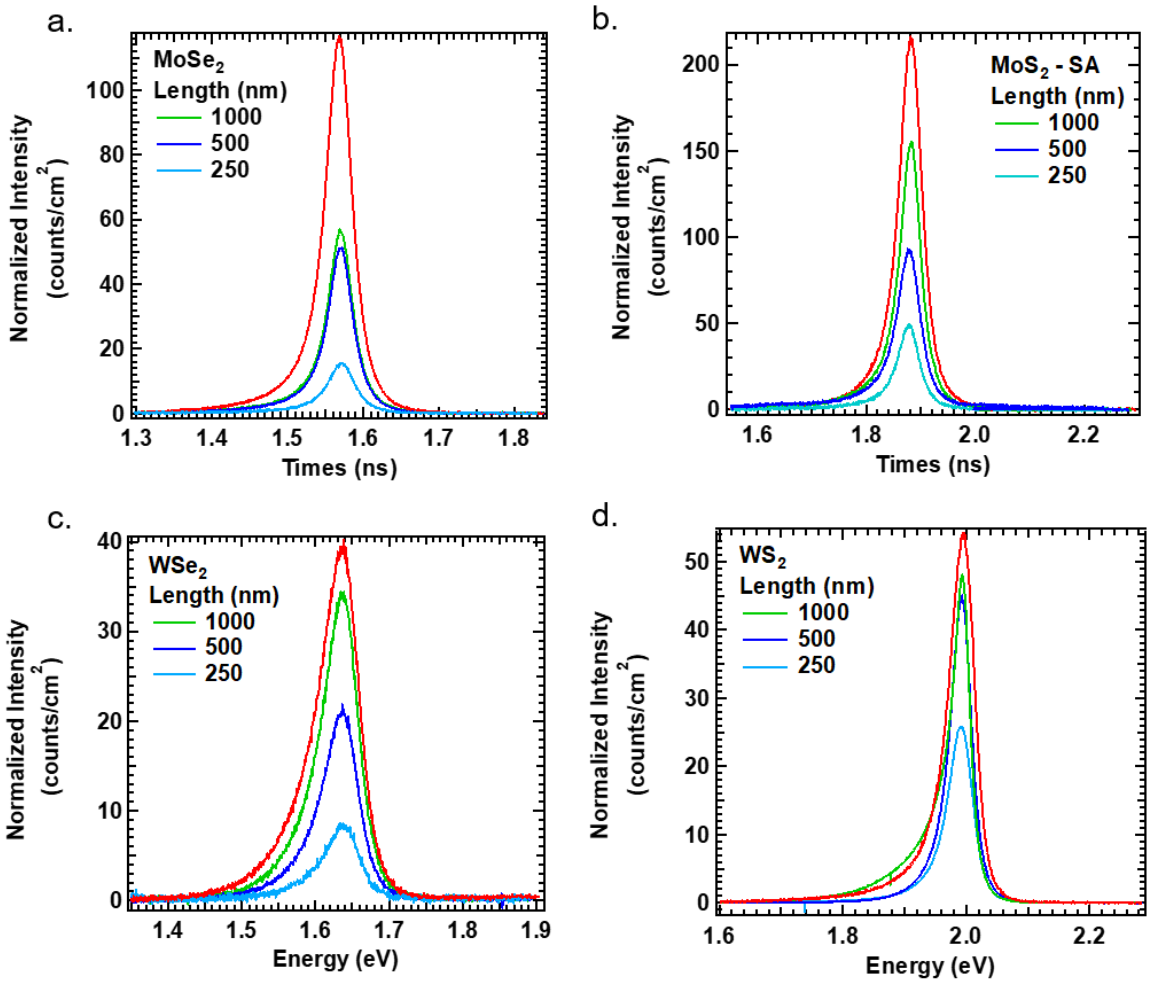

Figure S2. Area normalized PL spectra of all four TMDs for all 3 sizes of interest. The red spectra in each graph signifies the intensity of a control monolayer without etching. The materials are a) $MoSe_2$ b) MoS_2 (with TFSI) c) WSe_2 and d) WS_2 respectively.

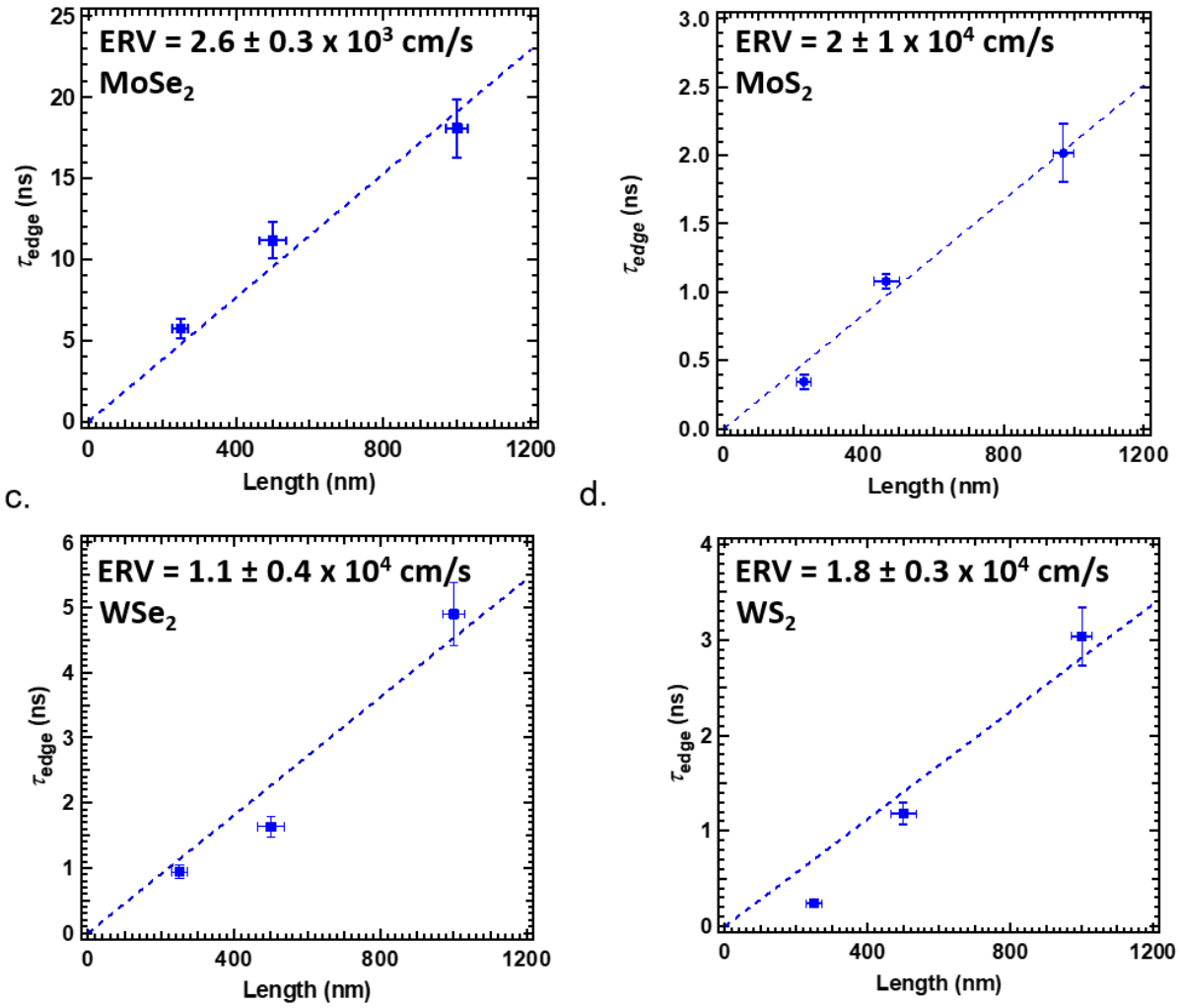

Figure S3. Extracted τ_{edge} of all four TMDs for all 3 sizes of interest. The materials are a) $MoSe_2$ b) MoS_2 (with TFSI) c) WSe_2 and d) WS_2 respectively. Note the significantly longer $MoSe_2$ edge lifetime reflective of its surface properties. Error bars signify the standard deviation of multiple samples of the same designed diameter.

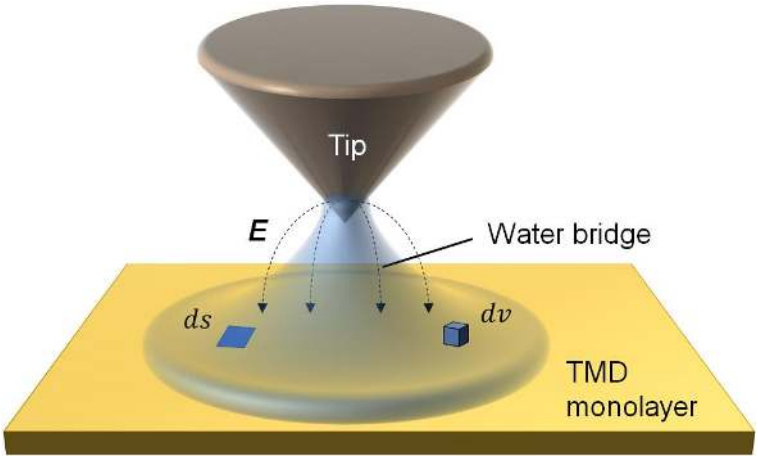

Figure S4. Illustration of the tip/water interface. *E* is the space-varying electrical field, *v* represents the volume of the condensed water, and *s* represents the surface area of the condensed water.

Materials Preparation and their Basic Properties

All 2D materials are purchased as bulk crystals. MoS_2 is purchased from SPi Supplies. All other 2D materials are purchased from HQ Graphene. The various materials are then exfoliated onto SiO_2/Si substrates and monolayers mapped via optical microscope. Multilayer films are thicker than 50 nm. The used materials are all 2H variants with semiconducting properties when made into field effect transistors. The surface defect density for each of the samples was reported in our previous work.[2]

ERV Derivation for Square Cross Sections

The methodology for finding the τ_{edge} expression is the same as in our previous work, and the process with the appropriate square boundary condition is detailed elsewhere (Shockley's recombination velocity derivation using a germanium filament).[3, 4] In this section, we compare Shockley's analytical model directly with our approximation of the τ_{edge} vs. ERV expression and check for percentage error. Accordingly, the exact expression for edge lifetime in relation to the recombination velocity is:

$$\frac{1}{\tau_{edge}} = 2D\left(\frac{\eta_o}{l}\right)^2 \quad (1)$$

$$\eta_o \tan(\eta_o) = \frac{\mathrm{ERV} * l}{D} \quad (2)$$

As shown above, D is the exciton diffusion coefficient, and η_o is the smallest solution to the diffusion equation (yielding the longest lifetime). Equation 1 originates from applying the

boundary condition of recombination velocity to all four edges of the square assuming uniform carrier distribution at $t = 0$. Equation 2 explicitly describes the solution's relation to ERV. Equation 1 and 2 becomes the approximation we used in the main text as:

$$\eta_o \tan(\eta_o) \rightarrow {\eta_o}^2 \qquad (3)$$

Assuming a D ~ 20 cm^2/s and upper limit of $l = 1\mu m$, at an ERV ~5 x 10^4 cm/s, the error between the two approximation is 8.5%.[5] At lower ERVs, the error decreases and equation (4) becomes a more accurate τ_{edge} vs ERV relation.

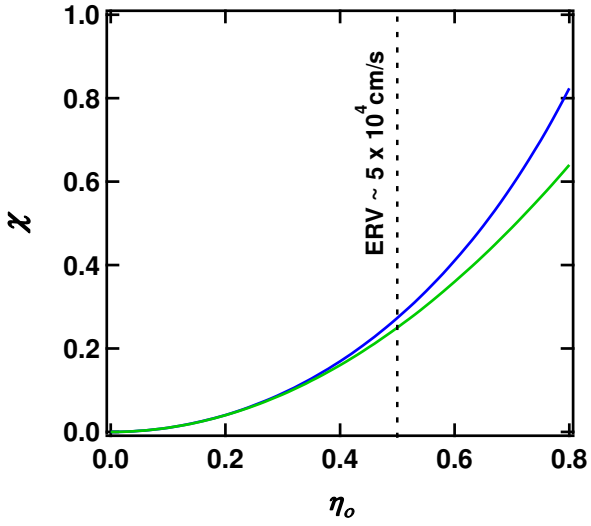

Figure S5 Graphic representation of deviation error. x-axis represents either $\eta_o{}^2$ (green) or $\eta_o \tan(\eta_o)$ (blue). At ERV = 5 x 10^4 cm/s, the error resulting from the approximation is ~ 8.7%. Smaller ERVs will only result in smaller error, reinforcing the validity of our approximation.

References

[1] G. M. Sacha, A. Verdaguer, M. Salmeron, *J. Phys. Chem. B* **2006**, 110, 14870-14873.

[2] P. Zhao, M. Amani, D.-H. Lien, G. H. Ahn, D. Kiriya, J. P. Mastandrea, J. W. Ager, E. Yablonovitch, D. C. Chrzan, A. Javey, *Nano Lett.* **2017,** *17*, 5356-5360.

[3] W. Shockley, *Electrons and Holes in Semiconductors with Applications to Transistor Electronics*. D. Van Nostrand Company Inc.: Princeton, New Jersey, 1950. P318-324

[4] R. Wang, B. A. Ruzicka, N. Kumar, M. Z. Bellus, H.-Y. Chiu, H. Zhao, *Phys. Rev. B* **2012,** *86*, 045406.

[5] M. Amani, P. Taheri, R. Addou, G. H. Ahn, D. Kiriya, D.-H. Lien, J. W. Ager, R. M. Wallace, A. Javey, *Nano Lett.* **2016,** *16*, 2786-2791.

Scanning probe lithography is used to pattern 2D semiconductors. It is a "clean" process for etching without leaving photoresist residues at the edge of the patterned monolayers, while quantifying the edge quality by edge recombination velocity. This work also highlights that it is possible to passivate the edges by chemical treatments as the edge are exposed without any residual coating.

Peida Zhao[1,2], Ruixuan Wang[1], Der-Hsien Lien[1,2], Yingbo Zhao[1,2], Hyungjin Kim[1,2], Joy Cho[1], Geun Ho Ahn[1,2], and Ali Javey[1,2]*

Scanning Probe Lithography Patterning of Monolayer Semiconductors and Its Application for Quantifying Edge Recombination